Determination of the complex refractive index segments of turbid sample with multispectral spatially modulated structured light and models approximation

Omri Meitav
Oren Shaul
David Abookasis

SPIE.

Determination of the complex refractive index segments of turbid sample with multispectral spatially modulated structured light and models approximation

Omri Meitav,[†] Oren Shaul,[†] and David Abookasis*
aAriel University, Department of Electrical and Electronics Engineering, Ariel 40700, Israel

Abstract. Spectral data enabling the derivation of a biological tissue sample's complex refractive index (CRI) can provide a range of valuable information in the clinical and research contexts. Specifically, changes in the CRI reflect alterations in tissue morphology and chemical composition, enabling its use as an optical marker during diagnosis and treatment. In the present work, we report a method for estimating the real and imaginary parts of the CRI of a biological sample using Kramers–Kronig (KK) relations in the spatial frequency domain. In this method, phase-shifted sinusoidal patterns at single high spatial frequency are serially projected onto the sample surface at different near-infrared wavelengths while a camera mounted normal to the sample surface acquires the reflected diffuse light. In the offline analysis pipeline, recorded images at each wavelength are converted to spatial phase maps using KK analysis and are then calibrated against phase-models derived from diffusion approximation. The amplitude of the reflected light, together with phase data, is then introduced into Fresnel equations to resolve both real and imaginary segments of the CRI at each wavelength. The technique was validated in tissue-mimicking phantoms with known optical parameters and in mouse models of ischemic injury and heat stress. Experimental data obtained indicate variations in the CRI among brain tissue suffering from injury. CRI fluctuations correlated with alterations in the scattering and absorption coefficients of the injured tissue are demonstrated. This technique for deriving dynamic changes in the CRI of tissue may be further developed as a clinical diagnostic tool and for biomedical research applications. To the best of our knowledge, this is the first report of the estimation of the spectral CRI of a mouse head following injury obtained in the spatial frequency domain. © *2017 Society of Photo-Optical Instrumentation Engineers (SPIE)* [DOI: 10.1117/1.JBO.22.9.097004]

Keywords: multispectral structured illumination; Hilbert transform; Kramers–Kronig relations; complex refractive index; absorption and scattering coefficients.

Paper 170431R received Jul. 3, 2017; accepted for publication Sep. 12, 2017; published online Sep. 28, 2017.

1 Introduction

Successful derivation of a biological tissue sample's complex refractive index (CRI) can serve a range of downstream diagnostic and research applications.[1–4] In the context of biophotonics, the real component of CRI (n) is related to the scattering coefficient (μ_s) while the imaginary part (k) is connected to the total attenuation coefficient (μ_{tr}), which is the sum of μ_s and the absorption coefficient, μ_a.[5] That is, by given n and k parameters, μ_s and μ_a coefficients can be indirectly deduced. Once these parameters or coefficients are obtained, they may be used in the clinical context as markers to diagnose metabolic states or pathological conditions, and monitor efficacy of therapeutic treatments. Specifically, k or μ_a reflects the process of light attenuation by physiologically relevant chromophores, such as hemoglobin, melanin, carotenes, lipids, water, etc., while n or μ_s reflects the structural variation of tissues largely attributed to changes in the concentration gradient between intra- and intercellular osmolarity.[6,7] The independent derivation of n and k values, as well as the determination of μ_s and μ_a, as a function of wavelength can provide a comprehensive battery of biochemical, morphological, and histochemical parameters of tissue.

The range of optical methods applied determine the optical properties of turbid materials may be broadly divided into direct and indirect techniques. Direct methods rely directly upon experimental results, without any model of photon migration. Indirect methods are more complicated in their use, involve mathematical models, and/or simulations of light propagation, and require sophisticated (and sometimes expensive) instrumentation.[8–11] Among techniques recently developed for optical characterization of turbid media and specifically for biomedical imaging is spatially modulated illumination, known also as spatial frequency-domain imaging.[12,13] With this technique, periodic illumination patterns (i.e., sinusoidal grid) at a range of spatial frequencies and excitation wavelengths are transmitted to the surface of a sample to separately map its intrinsic optical parameters over a wide field-of-view in a noncontact and scan-free fashion. The advantages of this imaging technique include: capability of depth sectioning, as well as wide-field and wild-range imaging, ease of use, and relatively low cost due to its minimal number of optical elements. The technical capabilities of this platform have been successfully demonstrated over the last 12 years, with successful demonstration in phantoms, animal, and human studies.[14–21] In the context of this technique, the present work aimed to apply structured illumination to estimate the real and imaginary component of turbid sample CRI in the near-infrared (NIR) spectral region (~650 to 1000 nm). However, as in conventional imaging platforms, the information regarding sample phase distribution is lost when recording the

---

*Address all correspondence to: David Abookasis, E-mail: davida@ariel.ac.il

†These authors contributed equally to this work.

diffuse reflectance by a camera. In order to retrieve phase data of biological samples from intensity measurements, several techniques and iterative computational algorithms have been developed to approach this fundamental challenge.[22–27] In this work, in order to derive the phase spectrum of biological sample from the amplitude of reflectance, Kramers–Kronig (KK) or the Hilbert transformation was employed.[28,29] Once the phase information is recovered, a set of equations based on Fresnel's reflection coefficient derived from classical electromagnetic theory[28,30] is used to obtain separately the real and imaginary part of the sample CRI value.

There are several approaches to derive sample refractive index, including refractometers, optical coherence tomography, total internal reflection, focused scanning microscopy, ellipsometry, etc., each with its own advantages and disadvantages.[31–33] However, the extraction of CRI information through spatially modulated illumination differs from the aforementioned methods and grants additional capabilities to this technique by enlarging its measurement range, as elaborated in this work.

The paper is set out as follows: in Sec. 2, we provide details of the system operation, data processing, tissue quantification analysis, and the animal model. Section 3 will be devoted to experimental results measured from both phantoms and the mice head experience models of injury. The calibration procedure to account for the system response will also be including in this section. Finally, in Sec. 4, we present a brief summary of results reported in this paper.

2 Methods

2.1 Optical Setup

The schematic diagram of the optical setup is illustrated in Fig. 1(a). The system consists of four main components: a modified commercial digital light projector (PLUS, U5-112), filter wheel (Thorlabs, FW102C) placed before the projector, a CCD camera (Guppy Pro, F-031B, AVT), and personal computer station, Intel® Core™2 Duo Processor E8500 running at 3.16 GHz with 4 GB memory. The wheel is equipped with four narrow bandpass filters centered at wavelengths of 690, 880, 920, and 970 nm (Thorlabs, FB Series, BW ± 10). At each wavelength, computer-generated sinusoidal patterns are serially projected onto the sample surface three times at each specific high spatial frequency of 0.27 mm^{-1}, at phase offsets of 0 deg, 120 deg, and 240 deg, respectively. A demonstration of these images projected onto the tissue phantom is presented in Fig. 1(b). The diffuse reflectance remitted from the sample is imaged onto a CCD camera (sequence of images), equipped with a zoom imaging lens system (Computar), and saved for processing and analysis offline. CCD exposure time is automatically adjusted for each sampled wavelength during the calibration process. The distance between the camera and the sample surface is 25 cm. Each single repetition lasting up to ∼60 s and included a total of 12 captured images: one spatial frequency ×
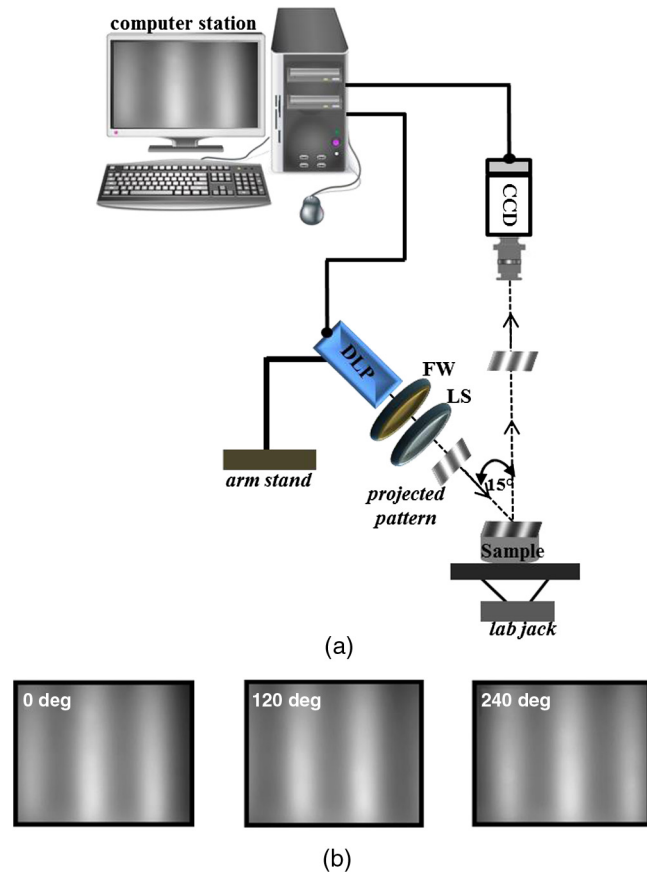

Fig. 1 (a) Schematic showing the optical system. DLP, digital light projector; FW, filter wheel; LS, lens system. (b) Example of structured light patterns projected onto tissue phantom as captured by the CCD camera.

three phases × four wavelengths. The entire setup is controlled by MATLAB software (MathWorks, Massachusetts), and imaging acquisition, synchronization, and data processing were carried out using in-house developed MATLAB scripts.

2.2 Data Processing

Prior to data analysis, the collected diffuse images were first normalized to the range between 0 and 1 using MATLAB code to overcome the nonlinearity of the camera quantum efficiency at the above wavelengths, after which the images were digitally filtered (fspecial) to eliminate high frequency noise originating from the camera itself during recording and to increase the signal-to-noise ratio. Then, a region-of-interest (RoI) was selected using the "imfreehand" function in MATLAB for further processing. The modulation amplitude of the diffusely reflected intensity (demodulated reflectance) RoI images at each wavelength, $R_d(\lambda_i)$, was approximated as follows:

$$R_d(\lambda_i) \propto \sqrt{[I_1(\lambda_i) - I_2(\lambda_i)]^2 + [I_1(\lambda_i) - I_3(\lambda_i)]^2 + [I_2(\lambda_i) - I_3(\lambda_i)]^2},$$

(1)

where $I_1(\lambda_i)$, $I_2(\lambda_i)$, and $I_3(\lambda_i)$ represent the captured adjacent reflectance images at spatial phases (phase shift) of 0 deg, 120 deg, and 240 deg, respectively, at the highest frequency.

Please note that by averaging the R_d images at each wavelength, the diffuse reflectance spectra of the sample can be derived. As mentioned previously, the information regarding sample phase

distribution, $\phi_d(\lambda_i)$, is lost when recording the diffuse reflectance and in order to derive the phase information, the KK or the Hilbert transformation is employed:[28,29]

$$\phi_d(\lambda_i) = \frac{\lambda_i}{\pi} \int_0^\infty \left(\frac{\ln[R_d(\lambda')/R_d(\lambda_i)]}{\lambda_i^2 - (\lambda')^2} \right) d\lambda'. \quad (2)$$

In this manner, the complete information (amplitude and phase) of the sample is obtained.

2.3 Properties Quantification Analysis

Once the phase information is recovered [Eq. (2)], a set of equations based on Fresnel's reflection coefficient at the interface of two materials derived from classical electromagnetic theory is used to obtain separately the real and imaginary part of the sample CRI value [$\mathbf{N}(\lambda) = n(\lambda) + ik(\lambda)$]:[28,30]

$$n(\lambda_i) = \frac{1 - R_d(\lambda_i)}{1 + R_d(\lambda_i) - 2 \cdot \sqrt{R_d(\lambda_i)} \cdot \cos[\phi_d(\lambda_i)]},$$

$$k(\lambda_i) = \frac{2 \cdot \sqrt{R_d(\lambda_i)} \cdot \sin[\phi(\lambda_i)]}{1 + R_d(\lambda_i) - 2 \cdot \sqrt{R_d(\lambda_i)} \cdot \cos[\phi_d(\lambda_i)]}. \quad (3)$$

In these equations, it is assumed that light is incident with an acute angle (<15 deg) from air to sample. Fresnel laws of reflection depend upon perpendicular or parallel light polarization [transverse electric (TE) or transverse magnetic (TM)]. Since the above equations assume light to be incident, with an acute angle (<15 deg, ~normal incidence) from air to the sample, the polarization state of light can be ignored. The electric and magnetic fields of an acute incident wave angle are both constantly tangential to the boundary, regardless of wave polarization. In order to reduce errors in the measurement of $R_d(\lambda_i)$ due to potential system variabilities (i.e., fluctuations and nonlinearity of projector light source, lens aberrations, and variable camera collection efficiency), we performed calibration with tissue-like phantoms of known optical properties over the near-infrared range.[34] The calibration utilized solid phantoms constructed from intralipid and dyes as reference standards.[35] Phantoms' optical properties over the wavelength range from 650 to 1000 nm were measured by oblique-incidence reflectometry.[36] The obtained spectral absorption and respective reduced scattering graphs were consistent with those determined by the two-distance steady-state frequency domain photon migration system used in Ref. 35. Calibration success was defined by reduction of the difference between the experimental reflectance R_d to that of a diffusion model theory for semi-infinite medium [Eq. (10), Ref. 37] by using the Levenberg–Marquardt algorithm in MATLAB. In this manner, we have a calibrated diffuse spectral reflectance cube with dimensions of $400 \times 400 \times 4$, where 400×400 is the 2-D image pixel size and 4 stands for the number of the wavelengths used. By scanning individual columns of the cube and performing the computation in Eq. (2), a phase matrix concomitantly is built, where each pixel in the matrix corresponds to the calculated phase, whereby the sample spatial phase distribution is reconstructed. Calculating the integral in Eq. (2) presents two challenges. First, the integral range extends from zero to infinity, covering an extremely wide wavelength region while, in practice, the spectrum is obtained over a finite bandwidth range, potentially affecting the accuracy of results. Second, there is a pole at $\lambda' = \lambda$, which requires an

approximation, typically by Maclaurin or double Fourier transform method.[38] In order to overcome these two problems, a second calibration procedure for the phase similar to the aforementioned was applied with R_d and compared against model theory [Eq. (11), Ref. 37]. The calibration process culminates in the derivation of two scale factors, $\vec{K}_{R_d}(\lambda)$ and $\vec{K}_{\phi_d}(\lambda)$, as estimators of the diffuse reflectance and phase, respectively. These factors are used later to multiply Eqs. (1) and (2) to derive optical properties of unknown samples. The above calibration procedure was performed immediately before and after each of the experiments in order to monitor system reliability and robustness. It should be stressed that it is not yet fully understood how the number of wavelengths measured affects the accuracy of phase calculation in Eq. (2). Practically speaking, the data range is unavoidably discrete and finite. Future study will be dedicated to better understand how this number of wavelengths measured affects the resulting n and k values, which is beyond the scope of the current work. Following the information of $n(\lambda)$ and $k(\lambda)$, the wavelength-dependent optical properties, such as the total attenuation (μ_{tr}) and reduced scattering (μ_s') coefficients, can be obtained as[3,5,39]

$$\mu_{tr}(\lambda) = \left(\frac{2 \cdot \pi}{\lambda} \right) k(\lambda), \quad \mu_s'(\lambda) = \left[\frac{n(\lambda)}{n_o} - 1 \right]^2 \xi, \quad (4)$$

where n_o is the refractive index of the medium and ξ is the proportionality factor related to particle size, wavelength, and particle density.[39] Since at high spatial frequency (typically > 0.1 mm^{-1}), we are primarily sensitive to scattering changes but are insensitive to absorption,[13,40–42] it can be assumed that $\mu_s'(\lambda)$ α $R_d(\lambda)$. High spatial frequency is analogous to small source–detector separation (SDS), in which the detected reflected light is dominated by shorter path length photons (short depth). On the contrary, large SDS is analogous to low-spatial frequency, in which the detected reflected light is dominated by longer path length photons (deeper depth); i.e., low spatial frequencies are maximally sensitive to absorption contrast. Along this line, the absorption coefficient is proportional to the diffuse reflectance, following $\mu_a(\lambda) \alpha - \log_{10}[R_d^{DC}(\lambda)]$,[43] where $R_d^{DC}(\lambda)$ is the diffuse reflectance when unmodulated ($f_x = 0$ mm^{-1}) light illuminates the sample. $R_d^{DC}(\lambda)$ can be derived from the spatially phase images by

$$R_d^{DC}(\lambda) = \frac{I_1 + I_2 + I_3}{3}$$
$$= \frac{I_o + I_o \exp(-120°) + I_o \exp(-240°)}{3} = I_o. \quad (5)$$

That is, with only three projected AC frames (I_1, I_2, I_3), sample optical parameters can be simultaneously derived. The workflow pipeline of these procedures is shown in Fig. 2. Please note that the reflectance data in Eqs. (1) and (5) were obtained by pixel-to-pixel operation performed upon three measured reflection images within the selected RoI. For each wavelength, measurements reflect a cube with dimensions of $X \times Y \times 3$, where $X \times Y$ is the 2-D RoI image pixel size and 3 stands for the phase shift number. A full treatment of relationships between diffuse reflectance and sample intensity may be found in Sec. 3.4 of Ref. 13. A noteworthy difference between the previous and current study lies in the calibration methodology [Eq. (23), Ref. 13].
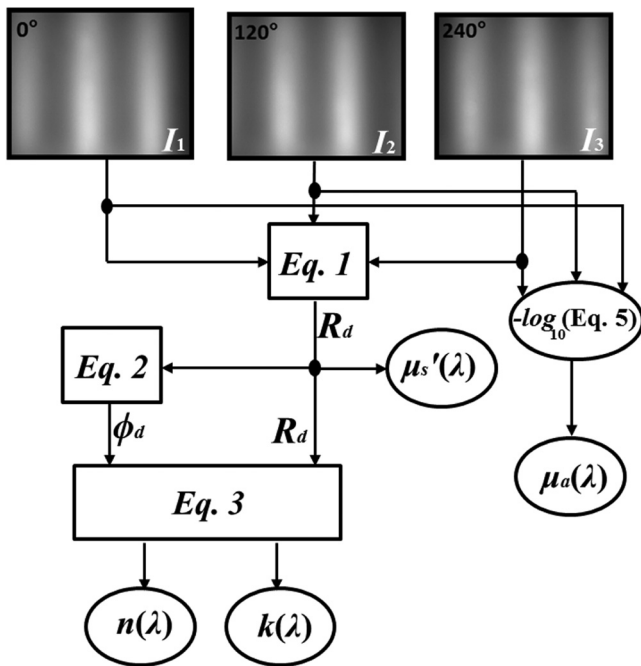
Fig. 2 Flowchart of the proposed algorithm for estimation of optical properties (μ_a, μ_s') and spectral CRI components (n, k). The flow steps are repeated for each repetition and wavelength.

2.4 Animal Model

A total of five adult male mice (C57BL/6, ~12 weeks, ~27 g) were used in the research: two mice experienced hypoxia due to ischemic brain injury induced by an overdose injection of xylazine (poisoning model), and the other three mice underwent heat stroke induced by increasing their body temperature up to 43°C using an in-house heat plate system. Body temperature was monitoring by thermocouple sensor (Lutron, TM-902C) and thermal camera (FLIR i7) positioned slightly off angle above the mouse head. The mice were housed in a research animal facility maintained at 22°C ± 2°C and relative humidity ~50%, placed under a 12-h reverse light/dark cycle with free access to food and water. Prior to each experiment, animals were anesthetized using a cocktail of ketamine (80 mg/kg) and xylazine (20 mg/kg) through intraperitoneal injection. Anesthetic depth was assessed periodically by the rear foot reflex. The animal's head was fixed, and scalp hair was removed with depilatory cream. Each mouse's baseline parameters serve as its own control, minimizing the number of animals required for this study. Animal procedures, care, and handling were approved by the Ariel University Animal Care and Use Committee (IACUC).

2.5 Statistical Analysis

The experimental results are presented as mean ± standard error $(\mu \pm \sigma)$, and two-way ANOVA was performed to determine significant differences, with a p-value <0.05 used as the significance cutoff. Calculations were carried out using MATLAB's Statistic Toolbox (MathWorks, United States). We would like to point out that although the head is a complex structure containing many tissue layers, in mice, these layers are very thin (skull ~ 500 μm, brain < 1 cm), and therefore, we consider the head as a homogenous medium. Hence, the results of the

recovered properties represent the averaged values from sampling of a single volume.

3 Results and Discussion

To demonstrate the utility of the above approach, experiments were first conducted on tissue phantoms and then on two mouse model of brain damage. Figure 3 presents results from a representative tissue phantom out of the six tested. The wavelength-dependence of the average real and imaginary parts of the CRI, along with their standard error, is plotted in Figs. 3(a) and 3(b), respectively. The data points in the graphs represent the mean and the bars refer to standard error over 10 repetitions during six nonconsecutive days of measurements. Error bars in some of the graphs are not seen because of minute deviation from the mean. The data were fitted based on the Cornu dispersion equation while corresponding imaginary indices were fitted to the power law equation:[1,5]

$$n(\lambda) = A + \frac{B}{\lambda - C}, \quad k(\lambda) = a \cdot \lambda^{1-b}. \quad (6)$$

The coefficient of each equation determined with the least-squares fitting procedure of the data was found to be: $A = 1.18$, $B = -7.34$, $C = -767.3$, $a = 7.66$, $b = 2.79$. λ is the wavelength in nanometers. Both graphs show monotonous spectral reduction correlating with increased wavelength as demonstrated elsewhere. In Fig. 3(a), the average of n across the wavelengths is ~1.25, in comparison to an anticipated refractive index of ~1.4. The ~11% difference may have several origins: (1) differential geometry employed for reflected light collection, (2) aberrations in light collection efficiency, (3) errors related to spatial frequency domain,[44,45] (4) utilizing few numbers of NIR wavelengths, and (5) approximations made using Eqs. (1)–(3). A correlation between the real and imaginary parts to the measured reduced scattering and total attenuation coefficients is presented in Figs. 3(c) and 3(d), respectively. In both graphs, a high positive Pearson correlation is observed. Finally, a strong positive correlation between the actual (reference) optical properties and measured (estimated) values is demonstrated for absorption [Fig. 3(e)] and reduced scattering [Fig. 3(f)] coefficients, respectively. The high positive correlation indicates good estimation of the true absorption/scattering coefficient value.

We next investigated the use of the technique with two clinically relevant mouse models of brain damage. Additional band-pass filters at wavelengths of 780 and 800 nm were added in these experiments. Figure 4(a) features a representative bare mouse scalp captured by the CCD camera at 690 nm with spatial frequency of 0.27 mm^{-1} at three phase shifts. Each captured reflectance image in the figure covers an area of 10×10 mm, corresponding to 200×200 pixels, resulting in an average spatial resolution of 0.05 mm/pixel. The selected RoI seen in the figure is between the anterior coronal suture (bregma) and posterior coronal suture (lambda). The wavelength-dependence of the real and imaginary indices obtained by our algorithm for hypoxia model is plotted in Figs. 4(b) and 4(c) and for the heat-stroke in Figs. 4(d) and 4(e), respectively. Heatstroke occurs when the body fails to regulate its own temperature and body temperature continues to rise. Usually, above 40°C, brain damage occurs and death follows if vigorous treatment is not instituted. The symbols in each plot are the experimental data points and the lines are fitted based on Eq. (6) to show the spectral dependence of n and k. The fitting coefficients of each equation (A, B, C, a, and b) based on Eq. (6), pre- and postinjury, were
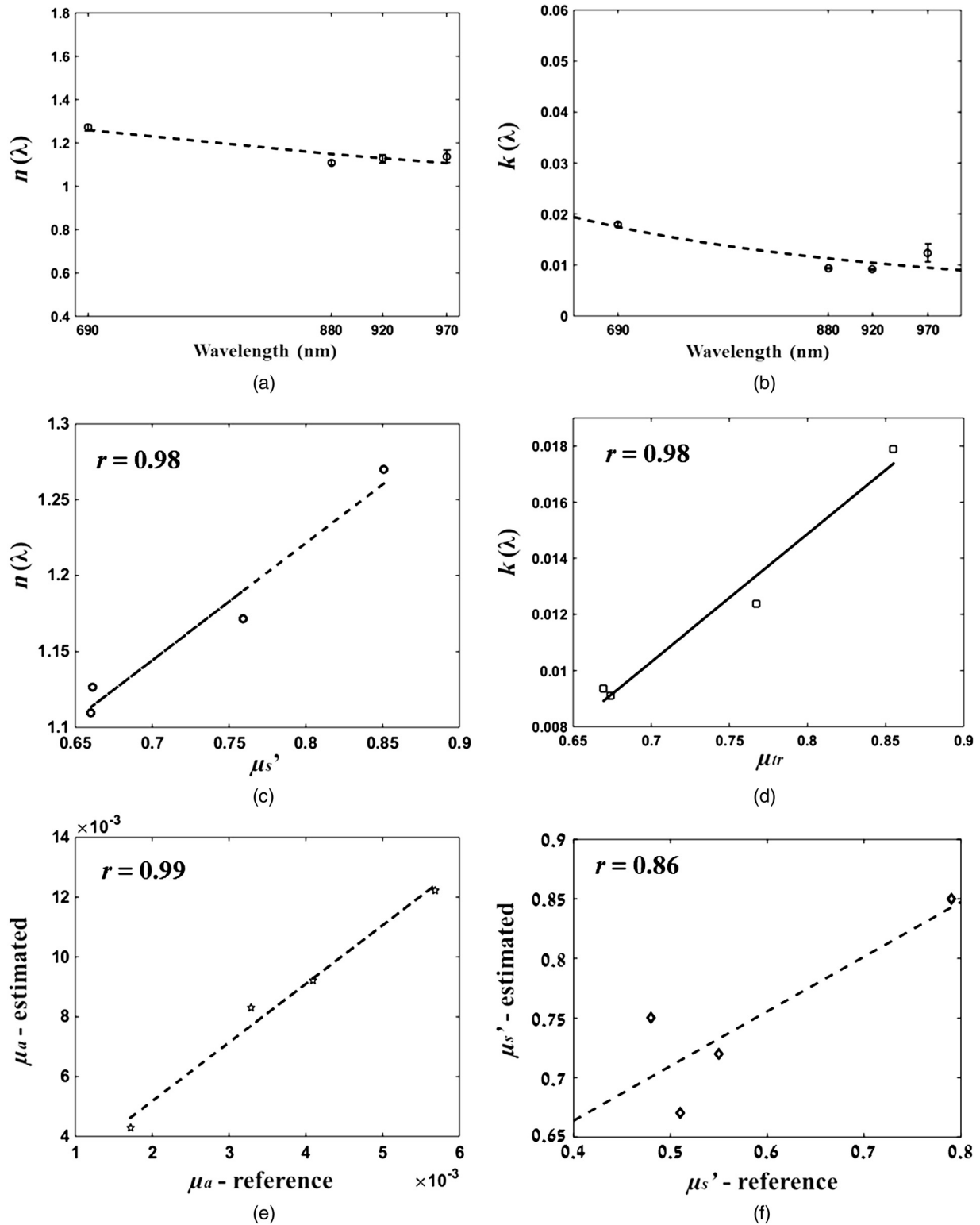
Fig. 3 Phantom experiment. (a) Real and (b) imaginary refractive indices plotted versus wavelength. Data points were fitted based on Eq. (6), respectively. Correlation of real or imaginary refractive indices, respectively, to (c) reduced scattering coefficient or (d) total attenuation coefficient. (e) Estimated (extracted) versus reference (expected) values of absorption and (f) reduced scattering coefficients derived from validation in tissue phantoms. The broken line represents the best-fit linear regression.

determined with the least-squares principle are presented in Table 1. The data in Fig. 4 and Table 1 demonstrate changes in tissue morphology [$n(\lambda)$] and hemodynamics [$k(\lambda)$], relative to baseline. In particular, since the real part of the CRI correlated with scattering, the variation we observed in $n(\lambda)$ reflects changes in the mean size, density, and distribution of cellular scattering substrates (cell membrane, nuclei, lysosomes, peroxisomes, mitochondria, and other organelles). Changes in the
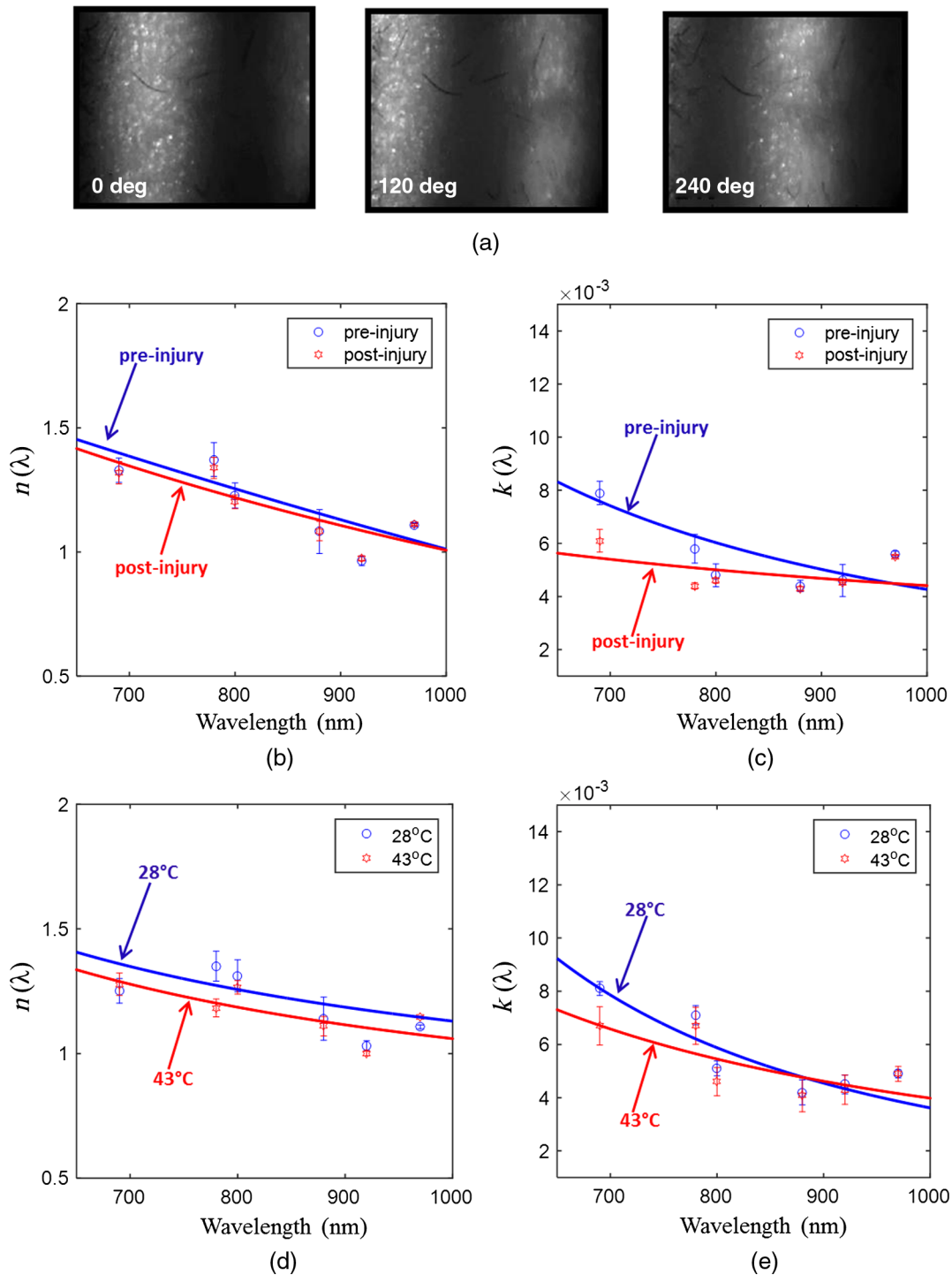
(a)

(b)

(c)

(d)

(e)

Fig. 4 (a) Three modulated images captured by the CCD camera from mouse scalp at single spatial frequency of $f_x = 0.27$ mm^{-1} at phase shifts of 0 deg, 120 deg, and 240 deg, respectively. RoI is selected between the anterior coronal suture (bregma) and posterior coronal suture (lambda). Real and imaginary refractive indices versus wavelength for hypoxia injury (b,c) and heatstroke (d,e), respectively of a representative mice. Data points represent the mean and a bar refers to standard error (correspond to the variation between RoI pixels). Error bars in some of the graphs are not seen because of minute deviation from the mean.

scattering characteristics of such subcellular bodies reflect cellular swelling and membrane damage (edema, leading to intracranial pressure elevation), a well-known mechanism observed in brain injury.[46,47] Generally speaking, common to all head injuries are excitotoxicity and oxidative stress mechanisms, primarily caused by excessive glutamate neurotransmission,

invoking a cascade of pathophysiological events leading to brain edema, increased intracranial pressure, and impaired cerebral perfusion (decreased blood flow), resulting eventually in neuronal cell death.[47-49] The imaginary part of the CRI reflects the total light attenuation, enabling derivation of hemoglobin concentration and oxygen saturation levels.[50,51] This variation

Table 1 Real and imaginary indices and their corresponding fit parameters based upon Eq. (6) in animal studies. Coefficients were obtained with wavelength in the unit of nanometers.

	$n(\lambda)$			$k(\lambda)$	
	A	B	C	a	b
Preinjury	−4	21633	−3317	190.6	2.55
Postinjury	−0.7	3090	−810.1	0.224	1.56
Pre-HS	0.65	459.60	42.88	12200	3.17
Post-HS	0.59	443.56	55.80	67.17	2.41

Note: HS, heatstroke.

in tissue biochemical composition can be explained by the fact that different molecules, such as hemoglobin, lipids, water, etc., absorb specific wavelengths of light, which alters the optical properties of tissue. The homeostatic response to brain damage includes decreased oxygen delivery to the brain inducing anaerobic metabolism and ATP depletion, potentially leading to permanent brain damage, neurological disorders, or even death.[52] This process affects both portions of the CRI, as reflected in the discrepancy between pre- and postinjury parameter values. The clearly distinguishable shift of the imaginary index [Figs. 4(c) and 4(e)], reflecting changes in both scattering and absorption coefficients, suggests the use of this index as an intrinsic contrast marker to distinguish between normal and injured brain tissues. We believe that more extensive experimental data and investigation of other dispersion formulas (i.e., Cauchy,

Conrady, Sellmeier[1,53]) may demonstrate more extensive shift in the real refractive index between normal and injury states. The overall changes in the optical properties correlating with body temperature elevation or xylazine-induced ischemia agree with previous studies.[54,55]

Figures 5 and 6 display a two-dimensional false-color map and its corresponding pixel histogram profile of the real and imaginary indices for the heatstroke and hypoxia models at a representative wavelength of 690 nm, respectively. The color bar to the right of each map indicates the corresponded value. Conversion of each index map into histogram distributions demonstrated localized changes in the CRI part levels at single-pixel resolution and illustrates its distribution within the field-of-view. The vertical axis in the histogram reflects the number of counts in each bin and the solid curve is a Gaussian fit with mean and standard deviation, respectively. As shown, histogram distribution indicates that pre- and postinjury states possess a characteristic peak value and distribution, which may serve as biomarkers of pathophysiological state. To further increase discrepancies before and after injury state and highlight tissue functional changes, we calculate the index variance from the mean gradient intensity ($\langle|\nabla n|^2\rangle$, $\langle|\nabla k|^2\rangle$) of the obtained maps that appears in Figs. 5 and 6. Results are given in Fig. 7. As demonstrated, changes up to 52% relative to baseline were detected, which emphasize the impact of injury upon CRI segments or indirectly on tissue morphology and composition. Therefore, in addition to above histogram characteristics, the mean gradient of the CRI segments may also serve as an informative optical biomarker of tissue condition.

As mentioned above, since at high spatial frequency we are primarily sensitive to scattering changes and therefore, $\mu_s'(\lambda)$ α
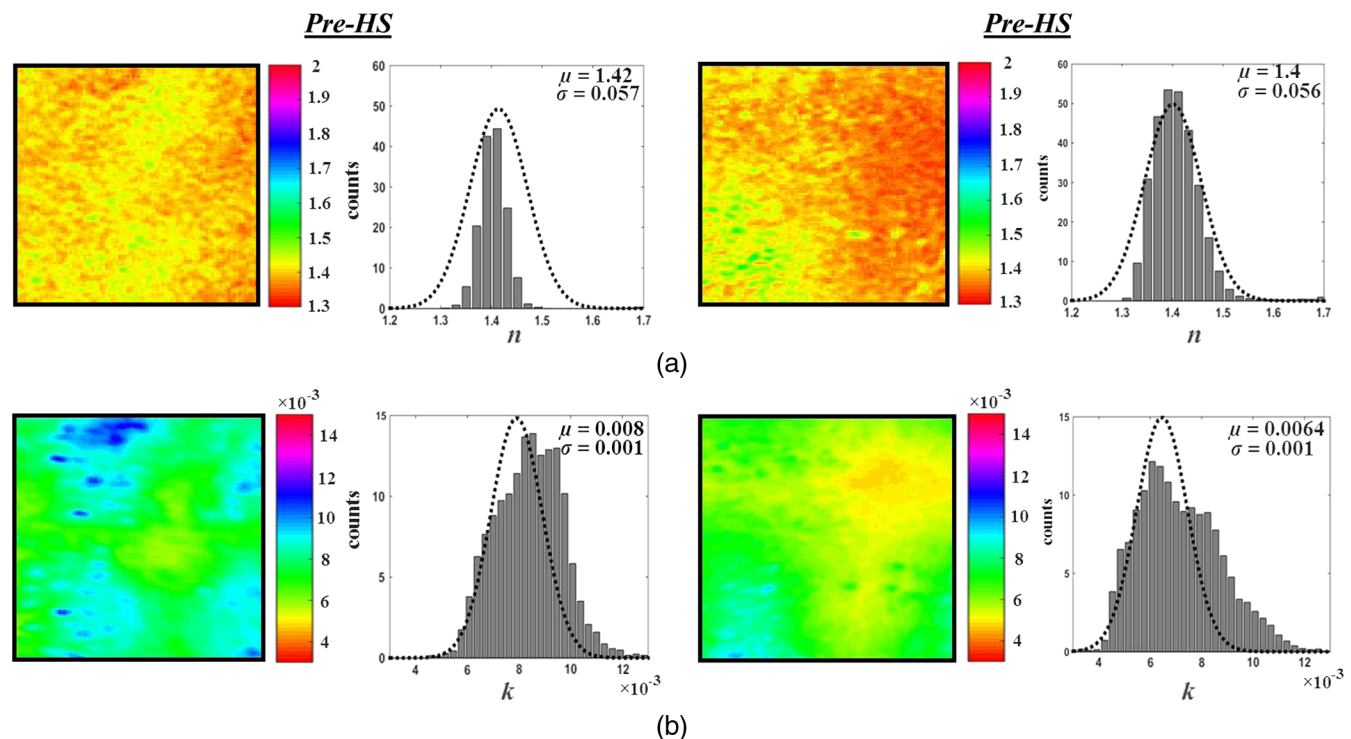

Fig. 5 Real (n) and imaginary (k) distribution maps with corresponding histogram (a) before and (b) after heatstroke onset. These maps were computed based on Eqs. (1)–(3). The horizontal color bar represents the value of each pixel in the map, such that higher index values correspond to brighter pixels. The vertical axis in each histogram reflects the number of counts in each bin and the solid curve in the histogram is a Gaussian fit with appropriate mean and standard deviation.

Pre-injury

Post-injury

(a)

(b)
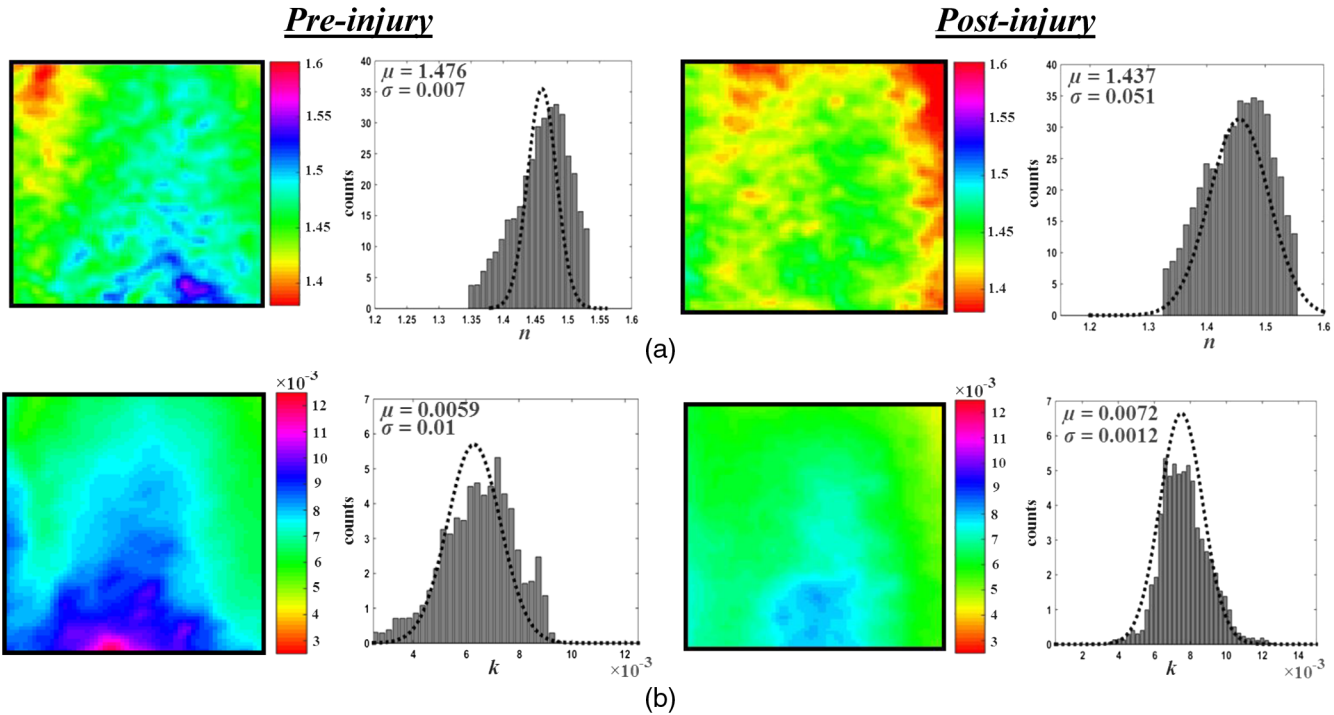
Fig. 6 Real (n) and imaginary (k) distribution maps with corresponding histogram (a) before and (b) after hypoxia onset. These maps were computed based on Eqs. (1)–(3). The horizontal color bar represents the value of each pixel in the map, such that higher index values correspond to brighter pixels. The vertical axis in each histogram reflects the number of counts in each bin and the solid curve in the histogram is a Gaussian fit with appropriate mean and standard deviation.

	$<|\nabla n|^2>$	
Pre-HS	0.1	
		Δ=22%
Post-HS	0.078	
Pre-injury	0.147	
		Δ=52%
Post-injury	0.07	

	$<|\nabla k|^2>$	
Pre-HS	5.1×10^{-6}	
		Δ=30%
Post-HS	3.56×10^{-6}	
Pre-injury	3.65×10^{-6}	
		Δ=50%
Post-injury	1.84×10^{-6}	

Fig. 7 Refractive indices variance calculated from the mean gradient intensity of the maps presented in Figs. 5 and 6, respectively, highlights changes in tissue morphology and composition following injury. The percent change for each possibility is given.

	A_s	
Pre-HS	8.13	
		Δ=37%
Post-HS	5.14	
Pre-injury	5.96	
		Δ=39%
Post-injury	3.64	

	sp	
Pre-HS	2.77	
		Δ=36%
Post-HS	1.77	
Pre-injury	2.02	
		Δ=38%
Post-injury	1.25	

Fig. 8 Scattering properties: amplitude—A_s and power—sp derived by Eq. (8). Changes more than 36% relative to baseline are demonstrated that highlights structural changes following injury. The percent change for each possibility is given. sp is related to mean size of the tissue scattering agents, while A_s is related to density and distribution of the same. HS: heatstroke.

$R_d(\lambda)$, information regarding scattering properties, namely, amplitude—A_s and power—sp can be derived by Mie theory.[56] The reduced scattering coefficient is characterized by an exponential monotone decrease relative to wavelength via the power law equation written as follows:[57,58]

$$\mu_s'(\lambda) = A_S \cdot \lambda^{-sp}. \tag{7}$$

By analyzing the spectra of scattered light, information regarding macroscopic cellular morphology can be retrieved through A_s and sp. In particular, sp is related to mean size of the tissue scattering agents (cell membrane, nuclei, lysosomes, peroxisomes, mitochondria, and other organelles in the cytoplasm) and defines spectral behavior of the reduced scattering coefficient, whereas A_s is related to density and distribution of scattering agents. Scattering parameters, pre- and postinjury, are presented in Fig. 8, which highlight structural changes more than 36% relative to baseline. The normalized reduced scattering spectra for each model pre- and postinjury are demonstrated in Figs. 9(a) and 9(b), respectively. The reduction in slope can be attributed to cellular and subcellular edema in response to injury.

4 Conclusion

To our knowledge, in this work we have described for the first time a practical method for estimating the wavelength-dependent CRI in the spatial frequency domain by projecting three sinusoidal patterns in the NIR spectral region. A set of assumptions and equations enabled the derivation of a range of tissue optical properties, such as the absorption and scattering indices, as well as the real and imaginary parts of the CRI. The above findings demonstrate proof-of-concept for the proposed methods on tissue phantoms and intact mouse scalp before and after different models of brain injury. Most notably, this is the first report we are aware of to calculate the spectral CRI of the intact mouse head during injury. We found that the imaginary index, which incorporates absorption and scattering to be highly sensitive to pathological states, identifying it as a candidate
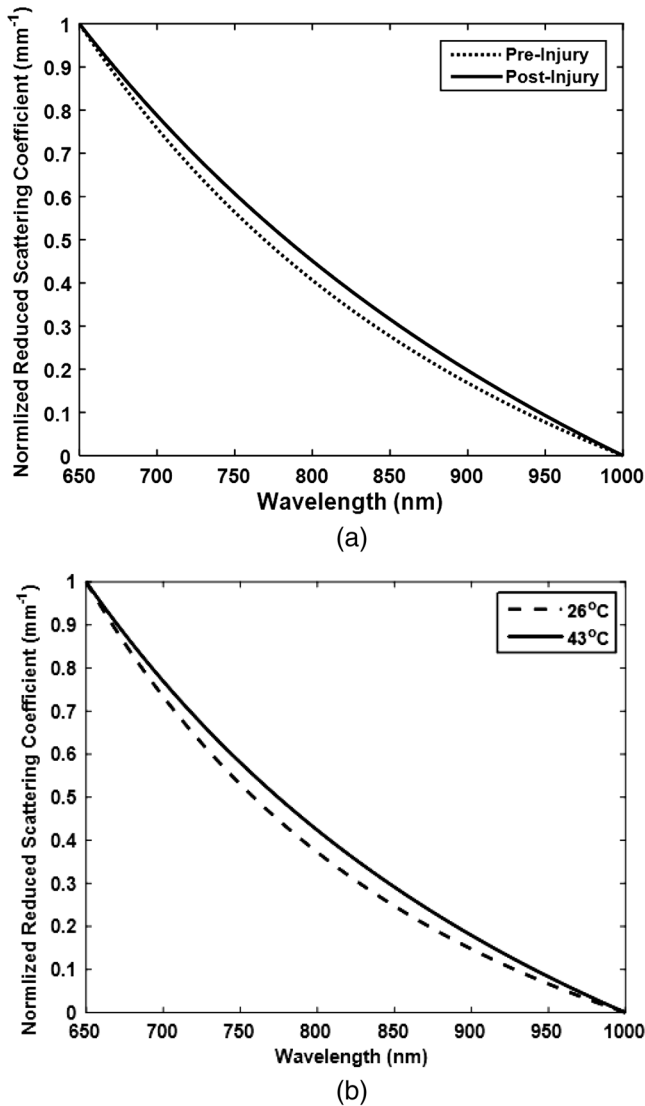
(a)

(b)

Fig. 9 Normalized reduced scattering spectra for hypoxia injury (a) and heatstroke injury (b). Reduction in the slope after injury in contrast to baseline can be explained by the changes in the average scattering particle size attributed to cellular and subcellular swelling in response to injury.

marker of pathological processes within brain tissue. Although analyses between mice are not presented and the reported results (Table 1, Figs. 4–9) are given for representative mice, similar trends in properties were observed for all mice involved in this work. Further experiments are currently under way to develop this finding with larger animal populations and by using a range of dispersion formulas to calculate the real refractive index, in order to further improve the algorithms' sensitivity. Future studies will be conducted with a larger number of wavelengths in order to increase the spectral resolution and accuracy of the CRI segments. While there are several approaches for retrieving information about the spectral CRI, the present work offers an easier, simpler, and lower-cost technique. The present method will be beneficial to the field of biophotonics during modeling light propagation in biological tissue and as a potential diagnostic tool and for monitoring medical treatment of neurological disorders, specifically for optical imaging systems operating in the spatial frequency domain.

Disclosures

The authors have no relevant financial interests in this article and no potential conflicts of interest to disclose.

References

1. H. Ding et al., "Refractive indices of human skin tissues at eight wavelengths and estimated dispersion relations between 300 and 1600 nm," *Phys. Med. Biol.* **51**(6), 1479–1489 (2006).
2. J.-C. Lai et al., "Complex refractive index measurement of biological tissues by attenuated total reflection ellipsometry," *Appl. Opt.* **49**(16), 3235–3238 (2010).
3. P. Giannios et al., "Complex refractive index of normal and malignant human colorectal tissue in the visible and near-infrared," *J. Biophotonics* **10**, 303–310 (2016).
4. T.-Q. Sun et al., "Measurement of complex refractive index of turbid media by scanning focused refractive index," *Opt. Lett.* **41**(16), 3767–3770 (2016).
5. P. Giannios et al., "Visible to near-infrared refractive properties of freshly-excised human-liver tissues: marking hepatic malignancies," *Sci. Rep.* **6**, 27910 (2016).
6. S. L. Jacques, "Optical properties of biological tissues: a review," *Phys. Med. Biol.* **58**(11), R37–R61 (2013).
7. V. V. Tuchin, *Handbook of Optical Biomedical Diagnostics*, SPIE Press, Bellingham, Washington (2002).
8. B. C. Wilson, M. S. Patterson, and S. T. Flock, "Indirect versus direct techniques for the measurement of the optical properties of tissues," *Photochem. Photobiol.* **46**(5), 601–608 (1987).
9. W. Cheong, S. A. Prahl, and A. J. Welch, "A review of the optical properties of biological tissues," *IEEE J. Quantum Electron.* **26**(12), 2166–2185 (1990).
10. M. S. Patterson, B. C. Wilson, and D. R. Wyman, "The propagation of optical radiation in tissue. II: Optical properties of tissues and resulting fluence distributions," *Lasers Med. Sci.* **6**(4), 379–390 (1991).
11. J. Falconet et al., "Estimation of optical properties of turbid media: experimental comparison of spatially and temporally resolved reflectance methods," *Appl. Opt.* **47**(11), 1734–1739 (2008).
12. D. J. Cuccia et al., "Modulated imaging: quantitative analysis and tomography of turbid media in the spatial-frequency domain," *Opt. Lett.* **30**(11), 1354–1356 (2005).
13. D. J. Cuccia et al., "Quantitation and mapping of tissue optical properties using modulated imaging," *J. Biomed. Opt.* **14**(2), 024012 (2009).
14. D. Abookasis et al., "Imaging cortical absorption, scattering, and hemodynamic response during ischemic stroke using spatially modulated near-infrared illumination," *J. Biomed. Opt.* **14**(2), 024033 (2009).
15. J. R. Weber et al., "Multispectral imaging of tissue absorption and scattering using spatial frequency domain imaging and a computed-tomography imaging spectrometer," *J. Biomed. Opt.* **16**(1), 011015 (2011).
16. A. J. Lin et al., "Spatial frequency domain Imaging of intrinsic optical property contrast in a mouse model of Alzheimer's disease," *Ann. Biomed. Eng.* **39**(4), 1349–1357 (2011).
17. S. Gioux et al., "First-in-human pilot study of a spatial frequency domain oxygenation imaging system," *J. Biomed. Opt.* **16**(8), 086015 (2011).
18. M. Laughney et al., "System analysis of spatial frequency domain imaging for quantitative mapping of surgically resected breast tissues," *J. Biomed. Opt.* **18**(3), 036012 (2013).
19. R. P. Singh-Moon et al., "Spatial mapping of drug delivery to brain tissue using hyperspectral spatial frequency-domain imaging," *J. Biomed. Opt.* **19**(9), 096003 (2014).
20. D. J. Rohrbach et al., "Characterization of nonmelanoma skin cancer for light therapy using spatial frequency domain imaging," *Biomed. Opt. Express* **6**(5), 1761–1766 (2015).
21. S. Nandy et al., "Characterizing optical properties and spatial heterogeneity of human ovarian tissue using spatial frequency domain imaging," *J. Biomed. Opt.* **21**(10), 101402 (2016).
22. P. Gao, G. Pedrini, and W. Osten, "Phase retrieval with resolution enhancement by using structured illumination," *Opt. Lett.* **38**(24), 5204–5207 (2013).
23. W.-S. Li et al., "Phase retrieval by using the transport-of-intensity equation with Hilbert transform," *Opt. Lett.* **41**(7), 1616–1619 (2016).

24. P. A. Ameen Yasir and J. Solomon Ivan, "Phase estimation using phase gradients obtained through Hilbert transform," *J. Opt. Soc. Am. A* **33**(10), 2010–2019 (2016).
25. P. Gemayel et al., "Cross-talk compensation of a spatial light modulator for iterative phase retrieval applications," *Appl. Opt.* **55**(4), 802–810 (2016).
26. Y. Xing, C. Quan, and C. J. Tay, "A modified phase-coding method for absolute phase retrieval," *Opt. Lasers Eng.* **87**, 97–102 (2016).
27. J. R. Fienup, "Phase retrieval algorithms: a comparison," *Appl. Opt.* **21**(15), 2758–2769 (1982).
28. J. L. Musfeldt, D. B. Tanner, and A. J. Paine, "Method for the determination of the optical properties of highly conjugated pigments," *J. Opt. Soc. Am. A* **10**(12), 2648–2657 (1993).
29. Y. Ben-Aderet et al., "Optical imaging of hidden objects behind clothing," *Appl. Opt.* **49**(20), 3926–3929 (2010).
30. M. Tasumi, *Introduction to Experimental Infrared Spectroscopy: Fundamentals and Practical Methods*, pp. 121–122, Wiley & Sons, West Sussex, UK (2015).
31. H. Liu et al., "Real part of refractive index measurement approach for absorbing liquid," *Appl. Opt.* **54**(19), 6046–6052 (2015).
32. J. Wang et al., "Measurement of the refractive index of hemoglobin solutions for a continuous spectral region," *Biomed. Opt. Express* **6**(7), 2536–2541 (2015).
33. Q. Ye et al., "Measurement of the complex refractive index of tissue-mimicking phantoms and biotissue by extended differential total reflection method," *J. Biomed. Opt.* **16**(9), 097001 (2011).
34. D. Abookasis, B. Volkov, and M. S. Mathews, "Closed head injury-induced changes in brain pathophysiology assessed with near-infrared structured illumination in a mouse model," *J. Biomed. Opt.* **18**(11), 116007 (2013).
35. F. Ayers et al., "Fabrication and characterization of silicone-based tissue phantoms with tunable optical properties in the visible and near infrared domain," *Proc. SPIE* **6870**, 687007 (2008).
36. J. Xia et al., "Monitoring sarcomere structure changes in whole muscle using diffuse light reflectance," *J. Biomed. Opt.* **11**(4), 040504 (2006).
37. A. Bassi et al., "Spatial shift of spatially modulated light projected on turbid media," *J. Opt. Soc. Am. A* **25**(11), 2833–2839 (2008).
38. K. Ohta and H. Ishida, "Comparison among several numerical integration methods for Kramers–Kronig transformation," *Appl. Spect.* **42**(6), 952–957 (1988).
39. J. S. Maier et al., "Possible correlation between blood glucose concentration and the reduced scattering coefficient of tissues in the near infrared," *Opt. Lett.* **19**(24), 2062–2064 (1994).
40. T. D. O'sullivan et al., "Diffuse optical imaging using spatially and temporally modulated light," *J. Biomed. Opt.* **17**(7), 071311 (2012).
41. S. C. Kanick et al., "Sub-diffusive scattering parameter maps recovered using wide-field high-frequency structured light imaging," *Biomed. Opt. Express* **5**(10), 3376–3390 (2014).
42. S. Gioux et al., "Three-dimensional surface profile intensity correction for spatially modulated imaging," *J. Biomed. Opt.* **14**(3), 034045 (2009).
43. A. J. Lin et al., "Visible spatial frequency domain imaging with a digital light microprojector," *J. Biomed. Opt.* **18**(9), 096007 (2013)
44. N. Bodenschatz et al., "Sources of errors in spatial frequency domain imaging of scattering media," *J. Biomed. Opt.* **19**(7), 071405 (2014).
45. Y. Zhao et al., "Angle correction for small animal tumor imaging with spatial frequency domain imaging (SFDI)," *Biomed. Opt. Express* **7**(6), 2373–2384 (2016).
46. J. J. Donkin and R. Vink, "Mechanisms of cerebral edema in traumatic brain injury: therapeutic developments," *Curr. Opin. Neurol.* **23**(3), 293–299 (2010).
47. C. O. de Oliveira, N. Ikuta, and A. Regner, "Outcome biomarkers following severe traumatic brain injury," *Rev. Bras. Ter. Intensiva* **20**(4), 411–421 (2008).
48. T. K. McIntosh et al., "Neuropathological sequelae of traumatic brain injury: relationship to neurochemical and biomechanical mechanisms," *Lab. Invest.* **74**(2), 315–342 (1996).
49. J. H. Yi and A. S. Hazell, "Excitotoxic mechanisms and the role of astrocytic glutamate transporters in traumatic brain injury," *Neurochem. Int.* **48**(5), 394–403 (2006).
50. T. H. Pham et al., "Quantifying the optical properties and chromophore concentrations of turbid media by chemometric analysis of hyperspectral diffuse reflectance data collected using a fourier interferometric imaging system," *Appl. Spect.* **55**(8), 1035–1045 (2001).
51. H. Z. Yeganeh et al., "Broadband continuous-wave technique to measure baseline values and changes in the tissue chromophore concentrations," *Biomed. Opt. Express* **3**(11), 2761–2770 (2012).
52. A. Zauner et al., "Brain oxygenation and energy metabolism: part I-biological function and pathophysiology," *Neurosurgery* **51**(2), 289–301 (2002).
53. B. Tatian, "Fitting refractive-index data with the Sellmeier dispersion formula," *Appl. Opt.* **23**(24), 4477–4485 (1984).
54. D. Abookasis et al., "Diffuse near-infrared reflectance spectroscopy during heatstroke in a mouse model: pilot study," *J. Biomed. Opt.* **17**(10), 105009 (2012).
55. I. Kofman and D. Abookasis, "Dual-wavelength laser speckle imaging for monitoring brain metabolic and hemodynamic response to closed head traumatic brain injury in mice," *J. Biomed. Opt.* **20**(10), 106009 (2015).
56. X. Wang et al., "Approximation of Mie scattering parameters in near-infrared tomography of normal breast tissue in vivo," *J. Biomed. Opt.* **10**(5), 051704 (2005).
57. R. Graaff et al., "Reduced light-scattering properties for mixtures of spherical particles: a simple approximation derived from Mie calculations," *Appl. Opt.* **31**(10), 1370–1376 (1992).
58. J. R. Mourant et al., "Mechanisms of light scattering from biological cells relevant to noninvasive optical-tissue diagnostics," *Appl. Opt.* **37**(16), 3586–3593 (1998).

Biographies for the authors are not available.